ACS Partner Journal

CHEM & BIO ENGINEERING

pubs.acs.org/ChemBioEng

Article

3D-Printing of Hierarchical Porous Copper-Based Metal–Organic-Framework Structures for Efficient Fixed-Bed Catalysts

Published as part of Chem & Bio Engineering virtual special issue "3D/4D Printing".

Ruizhe Xing,* Renliang Huang,* Rongxin Su, Jie Kong, Michael D. Dickey,* and Wei Qi

Cite This: *Chem Bio Eng.* 2024, 1, 264–273

Read Online

ACCESS | Metrics & More | Article Recommendations | Supporting Information

ABSTRACT: Metallic structures with hierarchical open pores that span several orders of magnitude are ideal candidates for various catalyst applications. However, porous metal materials prepared using alloy/dealloy methods still struggle to achieve continuous pore distribution across a broad size range. Herein, we report a printable copper (Cu)/iron (Fe) composite ink that produces a hierarchical porous Cu material with pores spanning over 4 orders of magnitude. The manufacturing process involves four steps: 3D-printing, annealing, dealloying, and reannealing. Because of the unique annealing process, the resulting hierarchical pore surface becomes coated with a layer of Cu–Fe alloy. This feature imparts remarkable catalytic ability and versatile functionality within fixed bed reactors for 4-nitrophenol (4-NP) reduction and Friedländer cyclization. Specifically, for 4-NP reduction, the porous Cu catalyst demonstrates an excellent reaction rate constant (k_{app} = 86.5 × 10^{-3} s^{-1}) and a wide adaptability of the substrate (up to 1.26 mM), whilst for Friedländer cyclization, a conversion over 95% within a retention time of only 20 min can be achieved by metal–organic-framework-decorated porous Cu catalyst. The utilization of dual metallic particles as printable inks offers valuable insights for fabricating hierarchical porous metallic structures for applications, such as advanced fixed-bed catalysts.

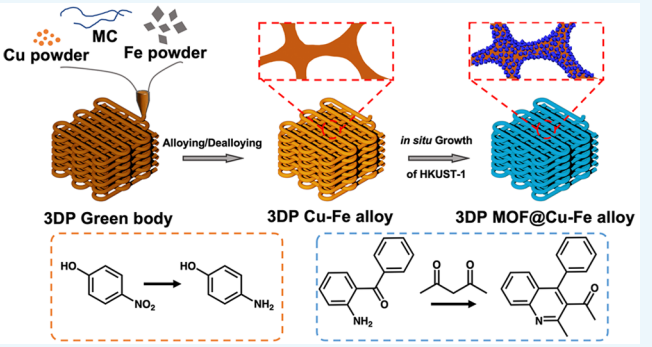

KEYWORDS: *3D-printed porous metal, direct ink writing, copper catalyst, 3D-printed MOF catalyst, 3D-printed fix-bed catalysts*

INTRODUCTION

Nanoporous metal catalysts have drawn tremendous attention[1] due to the large surface area of interconnected small pore channels that provide a high density of active sites for reactions.[2] Meanwhile, the excellent thermal and electrical conductivities of metals facilitate the timely and steady state transfer of heat generated by the reactions. Such materials show great potential in thermal-catalysis,[3] photocatalysis,[4] and electrocatalysis.[5−7] However, in a continuous flow reactor, a narrow pore size distribution will cause a dramatic increase in pressure drop and maldistribution of reactants, which leads to a nonuniform contact of the reactant with catalytic surface and channeling at the reactor wall boundary. Hierarchical structures—like those found in nature such as the human vascular and respiratory system—use nano-to-macropore size distribution to overcome these transport limitations while retaining high surface area.[8]

Previous efforts to fabricate hierarchical porous metals have attempted to use multiple annealing and re-/dealloying steps[7,9] or polymer templates.[10] However, these methods still face limitations in achieving wide spanning pore sizes, material versatility, and more importantly, the ability to fabricate ordered and anisotropic structures. These ordered and anisotropic structures are necessary for tailoring reactor geometry and controlling flow behavior for emerging applications such as advanced catalytic reactors, flow batteries, and catalytic robots.[11] As opposed to the conventional methods, it has been reported recently that nanoporous gold catalyst with a controlled pore size distribution from 30 to 1000 μm can be fabricated using a combination of three-dimensional (3D)-printing and dealloying processes.[3] This combination of "bottom-up" and "top-down" routes provides a new way of obtaining a complex hierarchical porous metallic catalyst. Nevertheless, gold is a precious metal, and its high cost presents a challenge for catalytic functionalization. Therefore, there is a need to explore a versatile system for the preparation of 3D-printed hierarchical porous non-precious

Received: January 3, 2024
Revised: February 13, 2024
Accepted: February 21, 2024
Published: February 26, 2024

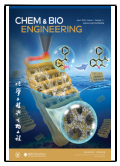

https://doi.org/10.1021/cbe.4c00001
Chem Bio Eng. 2024, 1, 264–273

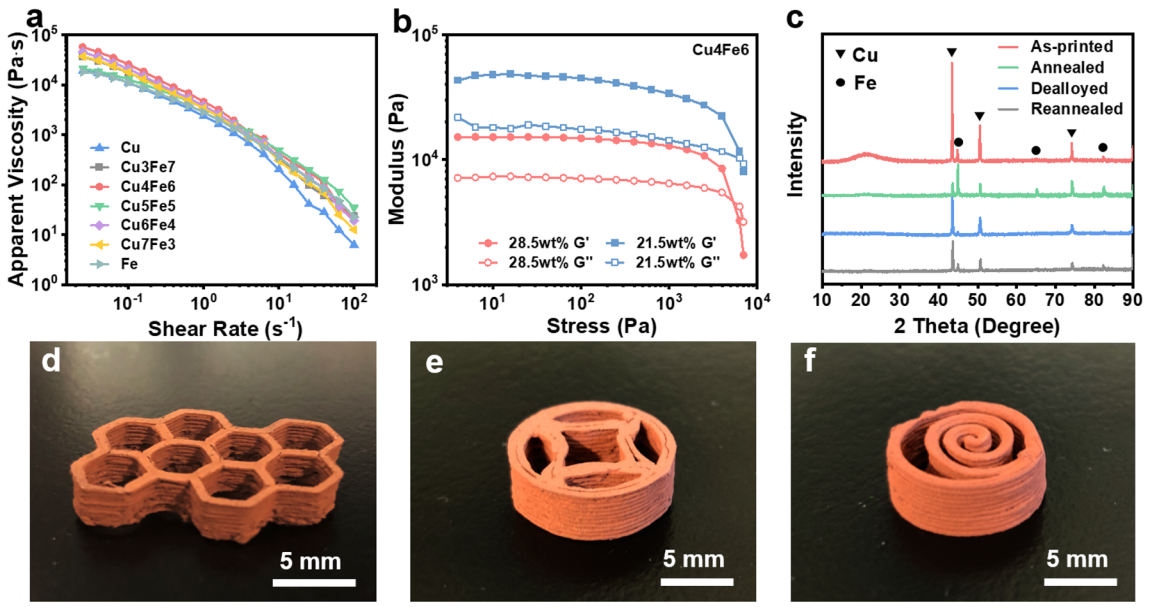

Figure 1. (a) Flow curves for Cu/Fe composite inks with different ratios of Cu/Fe. (b) Oscillatory rheological behavior for Cu_4Fe_6 composite ink. (c) XRD patterns after each preparation step (triangle, copper lattice; circle, iron lattice). 3D printed Cu/Fe composite with different geometries: (d) honeycomb, (e) star-shaped packing, and (f) spiral-shaped packing.

metals (e.g., iron and copper) while imparting them with excellent functional compatibility.

Recently, 3D-printing techniques have gradually emerged as a novel and popular technique in the field of catalysis. The ability to rapid prototype user-defined features combined with the ability to apply a wide range of functional materials have made 3D-printing techniques outstanding in reactionware design,[12] catalyst engineering,[3,13] and reaction modeling.[14] To enhance the reaction efficiency, efforts have been made to directly print three-dimensional architectures with engineered mass and heat transfer characteristics.[15] However, the resolution of 3D-printing limits these enhancements. Recently, high-resolution 3D-printing technologies, such as laser assisted printing, created porous metals with features as small as a few hundred microns, but the application of high-energy lasers is prone to result in the catalyst surface being dense and of low chemical activity.[6,16,17] Hence, the direct construction of different catalytic sites in 3D-printed porous metallic monoliths is still a challenge. Likewise, the incorporation of open channels at a 10−100 μm scale in the 3D-printed metallic parts still remains a challenge. Such structures can effectively reduce the pressure drop barrier and mass transfer limitations, especially for liquid flow reactors.[18]

Herein, we report a novel 3D-printing Cu/Fe composite ink that produces hierarchical porous Cu structures with pore size spans over 4 orders of magnitude. Such metallic parts are derived by a simple 4-step fabrication strategy: 3D-printing, annealing, dealloying, and reannealing. The printing ink is composed of Cu and Fe particles with different particle sizes. This allows for the fusion of Cu particles and partial alloying of Cu and Fe during the annealing process by controlling the solid diffusion length. Subsequent dealloying results in the pore surface covered with a layer of Cu−Fe alloy that has remarkable catalytic ability and versatile functionality. As an example, metal−organic frameworks (Cu-BTC) were successfully grown onto the porous Cu structures in the presence of only ligand solution. The hierarchical porous structure promotes the mass transfer between the reactants and active sites and enhances back-mixing, thereby greatly improving the catalytic efficiency in fixed bed reactors. The catalytic performances are then demonstrated in two types of fixed bed reactors for the reduction of 4-nitrophenol (4-NP) reduction and Friedländer cyclization.

RESULTS AND DISCUSSION

3D-Printing of Cu/Fe Composite Green Body. To prepare 3D-printed hierarchical porous Cu, we first formulated rheological modified viscoelastic Cu/Fe ink composed of a mixture of Cu (average size: 500 nm) and Fe particles (average size: 25 μm) (Figure S1) with different atomic ratio. We choose methylcellulose (MC) as the organic binder because of its good affinity to metal powders, mild degradation temperature, and low carbon residue postpyrolysis. The resulting inks are paste-like suspensions with extremely high viscosity. The ink experiences a shear thinning effect when passing through the nozzle, where the shear rate is highest (Figure 1a). This property facilitates the 3D-printing of the ink. The ink can be printed across a range of compositions since altering the molar ratio of Cu and Fe with an equivalent total mass loading does not significantly impact the viscosity and shear-thinning behavior of the ink. The water content greatly influences the rheological properties of the ink; Figure 1b compares the behavior of the two different water concentrations. Higher water content causes the yield stress to decrease, which significantly deteriorates the ability to print the ink into stable shapes. The yield stress of the composite ink with 28.5 wt % water is smaller than the one with 21.5% water, and the plateau storage modulus decreases by one order of magnitude. Higher content of water also leads to an increase in the shrinkage after the green body dries (Figure S2), which can cause cracking or failure. It is also worth noting that inks with water content smaller than 21.5 wt % become too viscous to be extruded through the printing nozzle (i.d. 300 μm). Therefore, in this work, we choose the water content of 21.5 wt % to enable printability while minimizing shrinkage. The corresponding rheological parameters are also in good agreement with those

https://doi.org/10.1021/cbe.4c00001
Chem Bio Eng. 2024, 1, 264−273

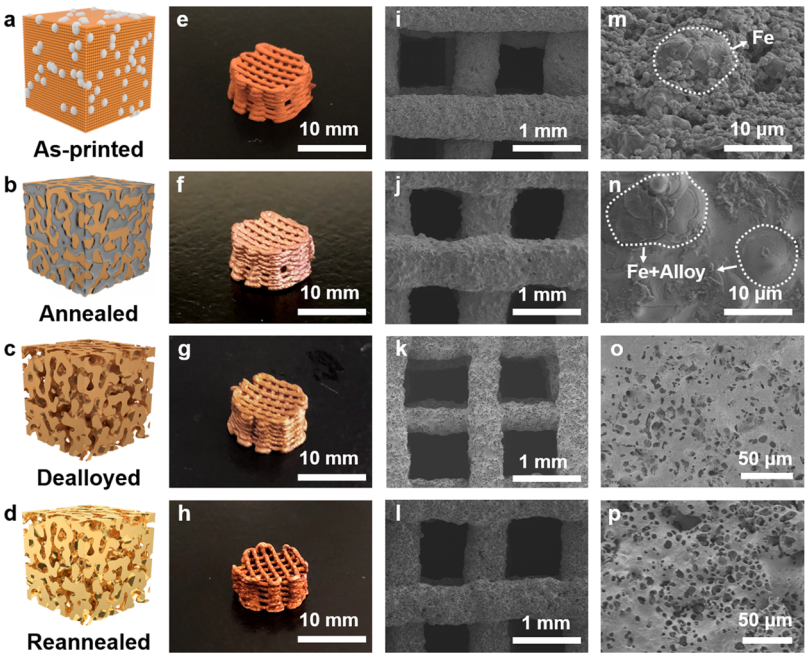

Figure 2. Schematic illustrations of the fabrication process of the hierarchical porous Cu sample (Cu4Fe6): (a) The as-printed Cu/Fe composite "green body". (b) The annealing step alloys the Fe and Cu phases from the interface and carbonizes the MC binder. (c) Hydrochloric acid selectively removes (dealloys) the Fe phase to yield pores. (d) Smoothing of the pore surface after reannealing. (e–h) Photographs of the woodpile-like architectures after printing, annealing, dealloying, and reannealing, respectively. (i–p) are the corresponding SEM images with different magnifications for each preparation step.

reported for other colloidal-ink-based 3D-printing techniques.[19]

To demonstrate the printability of Cu/Fe inks, we printed out different architectures used as fixed-bed packings. The printed parts came out nicely with a well-aligned layer-by-layer stacking profile (Figure 1d–f, and Figure 2e). Further observation under SEM (Figure 2i) reveals that the printed filament has a perfectly cylindrical shape and the filament diameter has a small deviation as well. Due to the significant particle diameter difference between Cu and Fe (~1:50), in the as-printed samples, Cu particles (smaller ones) tend to cover the Fe particles, leading to a state where Fe particles are dispersed in a matrix of Cu particles (Figure 2a,i,m).

Formation of Hierarchical Porous Cu Structure from Printed Cu/Fe Composite. To obtain the hierarchically porous Cu catalyst, post-treatments are performed. As depicted in Figure 2b–d, the printed Cu/Fe "green" part underwent the following annealing, dealloying, and reannealing process. After annealing in an argon atmosphere, the Cu/Fe green part turned light brown with a metallic luster consistent with alloy formation (Figure 2f). By annealing at 1100 °C for 6 h, the Cu particles fully sinter while also preventing the Fe particles from being fully alloyed with the Cu. The latter is important to avoid the formation of only nanopores during the dealloying step[17] (Figure 2j,n). We chose 1100 °C as the annealing temperature to achieve partial alloying of Cu and Fe as quickly as possible near the Cu–Fe liquidus line while ensuring that the printed structure does not collapse due to complete liquefaction. After annealing, the partially alloyed sample was submerged in 3 M HCl solution for a dealloying process where unalloyed Fe was preferentially dissolved, leaving large pores among the Cu matrix (Figure 2k,o). After dealloying, the sample appeared brownish (Figure 2g). Due to the loss of Fe particles, the Cu skeleton contains defects, which leads to weak mechanical performance with a compressive strength of 4.93 MPa (they could fail by applying pressure by hand). Therefore, a reannealing process was carried out at 850 °C for 3 h. Reannealing merges the small pores (<100 nm), thus forming a stronger network. Meanwhile, pores with diameters above 100 nm are nearly unaffected (Figure 2h,l,p). The mechanical performance is also greatly improved with the compressive strength of the printed woodpile lattice reaching 19.89 MPa (Figure S3).

Interestingly, under scanning electron microscopy-energy-dispersive spectrometry (SEM-EDS) (Figure 3f–i), we found that, after reannealing, there are still significant rich Fe signals inside pores, which indicates that Fe particles are not fully etched away. After dealloying, the inner walls of the pores present nanoscale "folds", but these topographical features disappear again after reannealing (Figure 3a–d). Elemental analysis of the inner walls shows that the atomic ratio of Fe to Cu after dealloying is nearly 1:1 (Figure S4). We propose a possible mechanism for the formation of hierarchical porous Cu from the perspective of diffusion kinetics. We make a first-order approximation that the Fe and Cu atom diffusion length (L) during annealing and reannealing processes follows Fick's law,

$$L = \sqrt{2D \cdot t} \tag{1}$$

in which D (cm^2/s) is the diffusion coefficient, and t is the diffusion time. The diffusion coefficient is derived from the following equation,

$$D = D_0 \exp\left(-\frac{E_a}{RT}\right) \tag{2}$$

where D_0 (cm^2/s) is the temperature-independent diffusion coefficient, E_a (kJ/mol) is the activation energy for diffusion. According to the literature, for the diffusion of Fe in Cu,

https://doi.org/10.1021/cbe.4c00001
Chem Bio Eng. 2024, 1, 264–273

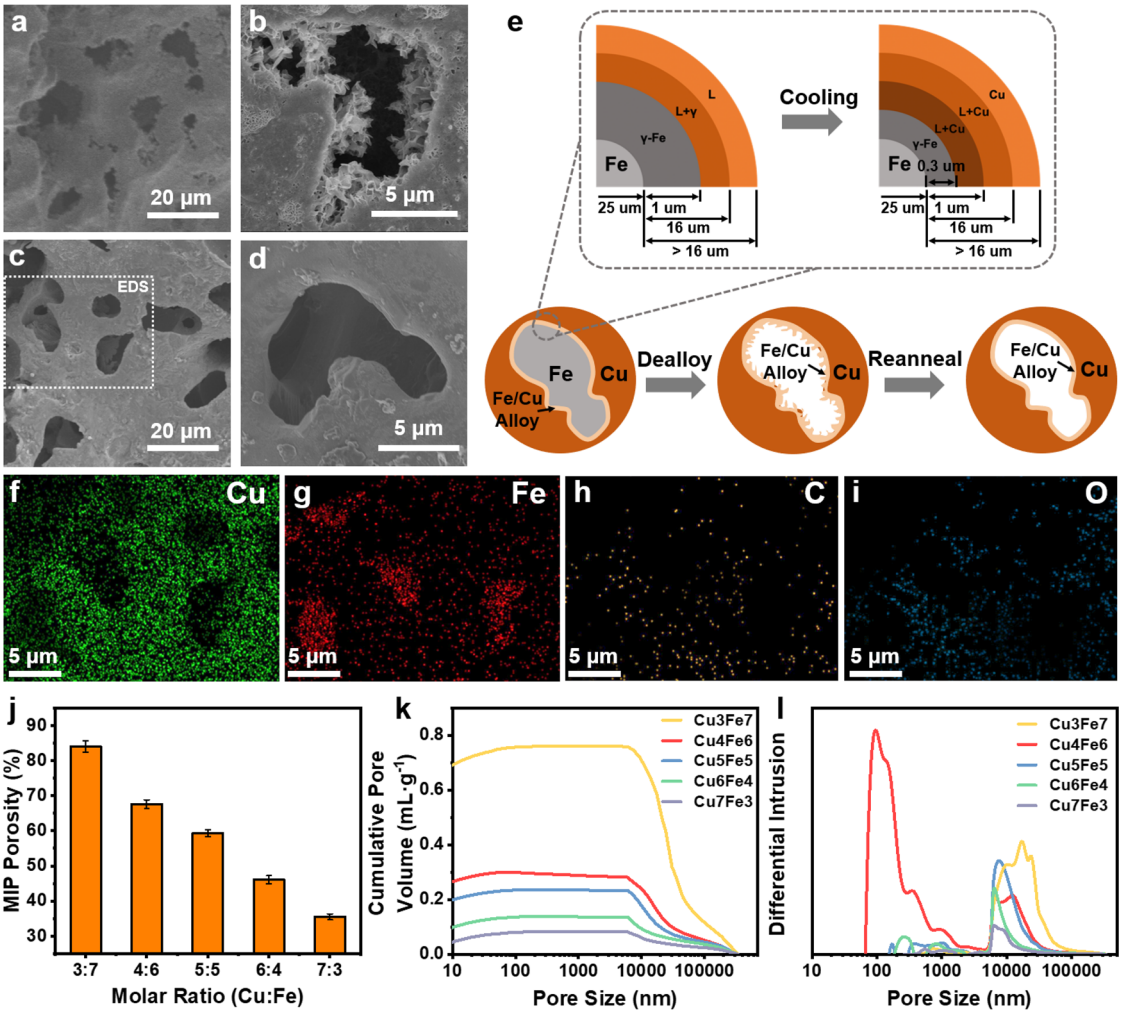

Figure 3. Characterization of the pore structure. SEM images depict microscale pore structures before (a,b) and after (c,d) the reannealing step with different magnifications. (e) Schematic illustration of the pore evolution during dealloying and reannealing steps. Note that the schematic is not to scale. (f–i) EDS mapping results of Cu, Fe, C, and O elements for reannealed sample (Cu4Fe6-R). The porosity (j), cumulative pore volume distribution (k), and pore size distribution (l) of the reannealed porous copper sample with different Cu/Fe molar ratios were determined by MIP analysis.

$D_{0,Fe\rightarrow Cu}$ is 0.504 and $E_{a,Fe\rightarrow Cu}$ is 208.2,[20] whereas for the diffusion of Cu in Fe, $D_{0,Cu\rightarrow Fe}$ is 0.57 and $E_{a,Cu\rightarrow Fe}$ is 238.6.[21] And for self-diffusion of Cu, $D_{0,Cu}$ is 0.468 and $E_{a,Cu}$ is 197.3.[22] Therefore, the diffusion length of Fe in Cu, Cu in Fe, and Cu in Cu at 1100 °C for 6 h are 17, 3, and 29 μm, respectively. In comparison, the average radius of Fe and Cu particles in the ink is 25 and 0.5 μm, respectively. Thus, after annealing, the Fe−Cu alloy may only form partially at the interface of Fe and Cu particles, with a continuous Cu phase surrounding it. Further observation of SEM echoes this theory (Figure 2n): the Cu particles merged together into a continuous and dense matrix; the Fe particles retain their original contour size, but typical alloy crystals can be clearly observed around Fe particles.

This alloying and the following dealloying process are also schematically illustrated in Figure 3e. Utilizing the second Fick's law, the theoretical model of diffusion concentration can be calculated as

$$\frac{\partial^2 c}{\partial z^2} + \left(\frac{2}{z} + 2z\right)\frac{\partial c}{\partial z} = 0 \quad (3)$$

where c is the concentration of metals and $z = r/(2\sqrt{Dt})$ is the dimensionless diffusion length. We take the center point of Fe particles to be zero, and the concentration of Fe and Cu elements at the Cu/Fe interface as a function of diffusion distance can be plotted (Figure S5b). When Cu diffuses into Fe, the concentration of Cu in Fe decreases by 50% when the diffusion distance is about 1 μm, whereas when Fe diffuses into Cu, the concentration of Fe decreases by only 10% at the same distance. Therefore, during the sintering process, it is presumable that the Fe content within about 1 μm near the surface is always higher than 90%. According to the Cu/Fe binary phase diagram (Figure S5a), when annealed at 1100 °C, this part of Fe (within 1 μm near the surface) tends to stay in the form of γ-Fe and Cu atoms that exist as a solid solution.

When the sample was further cooled in the furnace, the region within 0.3 μm of the Fe surface maintains its γ form, as can be inferred from the phase diagram (Figure S5a), while the region between 0.3 and 1 μm is likely to transform into the form of Cu dispersed in the liquid phase of Cu−Fe alloy (L +Cu). Compared to γ-Fe, Cu−Fe alloy has a higher cohesion energy which leads to a much slower dissolution rate in the presence of acid.[23] Therefore, after immersion in HCl solution,

https://doi.org/10.1021/cbe.4c00001
Chem Bio Eng. 2024, 1, 264−273

Fe is preferentially etched away, leaving behind the Cu−Fe alloy inside the walls of the pores. This folded, wavy geometry presumably originates from the recrystallized γ-Fe crystals during cooling. It can be seen under SEM that the depth of this folded structure is about 0.2−0.5 μm, which is consistent with the theoretical thickness of γ-Fe, 0.3 μm (Figure 3b, Figure S4). After reannealing at 850 °C, the alloy phase turns back to liquid, while the bulk Cu framework stays solid. Thus, the alloy phase coats inside the pores due to the wetting behavior, resulting in a smoothed pore structure (Figure 3d).

X-ray diffraction (XRD) tests were also performed to track the crystal changes of 3D-printed hierarchical porous Cu (Figure 1c). The peaks at 2 theta of 43.38°, 50.52°, and 74.18° correspond to the (111), (200), and (220) crystal planes of Cu (PDF#04-0836). Whereas the peaks at 2 theta of 44.74°, 65.08°, and 82.36° correspond to the (110), (200), and (211) crystal planes of Fe (PDF#006-0696). Due to the smaller Cu particles surrounding the Fe particles and blocking the X-ray, the diffraction peaks of Fe are much weaker than those of Cu. After annealing, Fe diffuses inside the Cu matrix; therefore, the peak intensity of Fe increases. The slight shifts of peaks at 2 theta of 43.55°, 50.64°, and 74.28° reveal the formation of Cu−Fe phases. After dealloying, Fe is largely consumed, which leads to a further decrease in the intensity of the Fe signal. After the reannealing process, the residual Fe redistributes on the pore surface, resulting in a slight increase in the intensity of the Fe signal.

The porosity can be easily tuned by varying the Cu/Fe ratio. The more Fe particles included in the ink, the greater the porosity of the final sample (Figure 3j). Cross-sectional SEM images reveal that when the Cu/Fe ratio reaches 3:7, the amount of Fe in the skeleton becomes too large, resulting in a poorly connected structure after dealloying, which then leads to inferior mechanical properties (Figure S6). The pore size distribution and total pore volume of each sample are listed in Figure 3k,l. The pore volume between 5 and 50 μm gradually increases with the increase of Fe content in the printing ink. However, we found that the pore size distribution between 0.1 and 5 μm increased significantly only when the molar ratio of Cu/Fe was 4:6. When the Fe content is low, Fe particles stay isolated from each other, so only the templated pore structure (>5 μm) will be formed; when the content of Fe becomes higher, the Fe particles can touch each other and even sinter together, resulting in a significant increase of large pore structures (5−100 μm) and total pore volume. When in a proper proportion (i.e., Cu/Fe = 4:6), the spacing between Fe particles would just be able to form small continuous pores during dealloying, leading to a rich pore size distribution at both nanoscale (100−1000 nm) and microscale (1−100 μm). The pores generated after dealloying are continuous. To prove this, we measured the porosity based on weight. As depicted in Figure S7, for a Cu/Fe ratio smaller than 5:5, the porosity aligns with the mercury intrusion porosimetry (MIP) results. This implies that during dealloying, solutions (continuous medium) can fully contact the Fe particles, thus creating an interconnected cavity.

3. 3D-Printed Self-Supported Cu Catalyst for Gravitational Fixed Bed Flow Reactor. The as-prepared hierarchical Cu (Cu4Fe6-R) has a rich porosity (>65%), wide pore size distribution (0.1−100 μm), and Cu−Fe alloy feature on the pore surface, showing great potential in catalytic applications. To demonstrate this, we first directly printed out a cylindrical woodpile structural catalyst and tested its catalytic efficiency in a model reaction, 4-nitrophenol (4-NP) reduction (Scheme 1). The reduction of 4-NP yields 4-aminophenol (4-AP), which is an important chemical intermediate widely used in industry.[24] 4-NP reduction mostly relies on noble metallic catalysts such as gold (Au), palladium (Pd), and silver (Ag).[25] Non-noble metallic catalysts, such as Fe, cobalt (Co), or tungsten oxides (WO_x), suffered from unsatisfied turnover frequencies (TOFs) and were limited to batch reactions. Here, we propose a highly efficient 3D-printed Cu catalyst (3DPCu4Fe6-R) for 4-NP reduction (Scheme 1) with a significantly improved continuous volumetric capacity. First, we tested the catalytic efficiency of 3DPCu4Fe6-R in a batch reaction system. We cut off and weighed a tiny piece of sample from 3DPCu4Fe6-R as the catalyst to achieve 0.5 mg/mL (mass catalyst/volume solution). UV−vis absorption was used to track the reaction conversion based on the standard absorption curve of 4-NP and $NaBH_4$ mixture (Figure S8). The disappearance of a peak at 400 nm indicates the consumption of 4-NP (Figure 4a). The apparent reaction kinetic constant (k_{app}) is 1.34×10^{-1} s^{-1} when the initial 4-NP concentration is set to 0.26 mM, a value that is within the range commonly used in the literature. This is a noteworthy reaction rate based on a batch reactor model, which may partially be attributed to the large dose of the catalyst (0.5 mg/mL). The TOF and k_{nor} reflect the catalytic efficiency per unit catalyst, and they are 4.284 h^{-1} and 0.268 $mL{\cdot}s^{-1}{\cdot}mg^{-1}$, respectively. These values are also comparable to those of the noble metallic catalysts reported in the literature (Table S2). When the initial 4-NP concentration is further increased to 1.29 mM, the k_{app} decreases sharply to 4.49×10^{-3} s^{-1} due to the saturated catalytic sites. But a good TOF of 0.991 h^{-1} and k_{nor} of 0.036 $mL{\cdot}s^{-1}{\cdot}mg^{-1}$ is still presented, indicating an intrinsic good catalytic efficiency of 3DPCu4Fe6-R. On the contrary, 3D-printed pure Cu catalyst (3DPCu10Fe0-R) shows barely any catalytic efficiency with a k_{app} being 0.19×10^{-3} s^{-1} (Figure 4b). With the decrease in the Cu/Fe ratio, the k_{app} gradually increases (Figure 4c). This implies that the unique Cu−Fe alloy structure on the pore surface could be the key to improve the catalytic efficiency.

Scheme 1

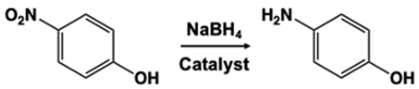

As shown in Figure 4f, we propose a possible mechanism for the 3DPCu4Fe6-R catalyst. According to the Langmuir−Hinshelwood model,[26] Cu(0) promotes the dissociation of the B−H bond and thus the formation of Cu−H intermediates by obtaining hydrogen atoms from $NaBH_4$. The Cu−H intermediate will then attack the positively charged nitrogen atom in 4-NP and form the corresponding amino group. The 3DPCu4Fe6-R catalyst has a rich pore structure and provides more adsorption sites for 4-NP substrates, thus speeding up the reaction. On the other hand, due to the presence of $NaBH_4$, the solution is moderately alkaline (pH >10), so Fe(III) would form by electrochemical corrosion, thereby poisoning the catalytic sites. However, for the 3DPCu4Fe6-R catalyst, Fe(II) would likely form due to the presence of Cu(0) and $NaBH_4$ on the pore surface. This process generates numerous Cu(0)/Fe(II) and Cu(0)/Fe(III) combinations, promoting the continuous absorption of hydrogen from the

https://doi.org/10.1021/cbe.4c00001
Chem Bio Eng. 2024, 1, 264−273

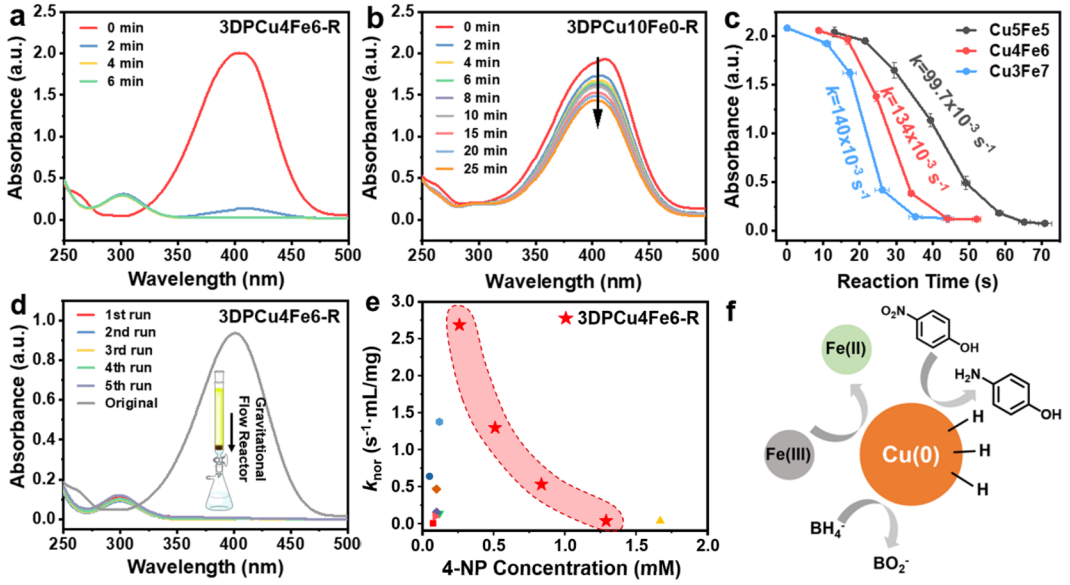

Figure 4. Time-dependent UV−vis spectra of 4-NP reaction liquid catalyzed by as-prepared Cu catalyst with a Cu/Fe molar ratio of (a) 4:6 and (b) 10:0, respectively. (c) Reaction kinetics curves for catalyst prepared with different Cu/Fe ratios. (d) UV−vis spectra of the solution before and after the reaction for five consecutive runs in the fixed-bed flow reactor. Inset figure: gravitational flow reactor set-up. (e) Comparison of the normalized kinetic constant with recent literature. (Detailed literature data can be found in Table S2.) (f) Schematic illustration of 4-NP reduction by the as-prepared porous Cu4Fe6 catalyst.

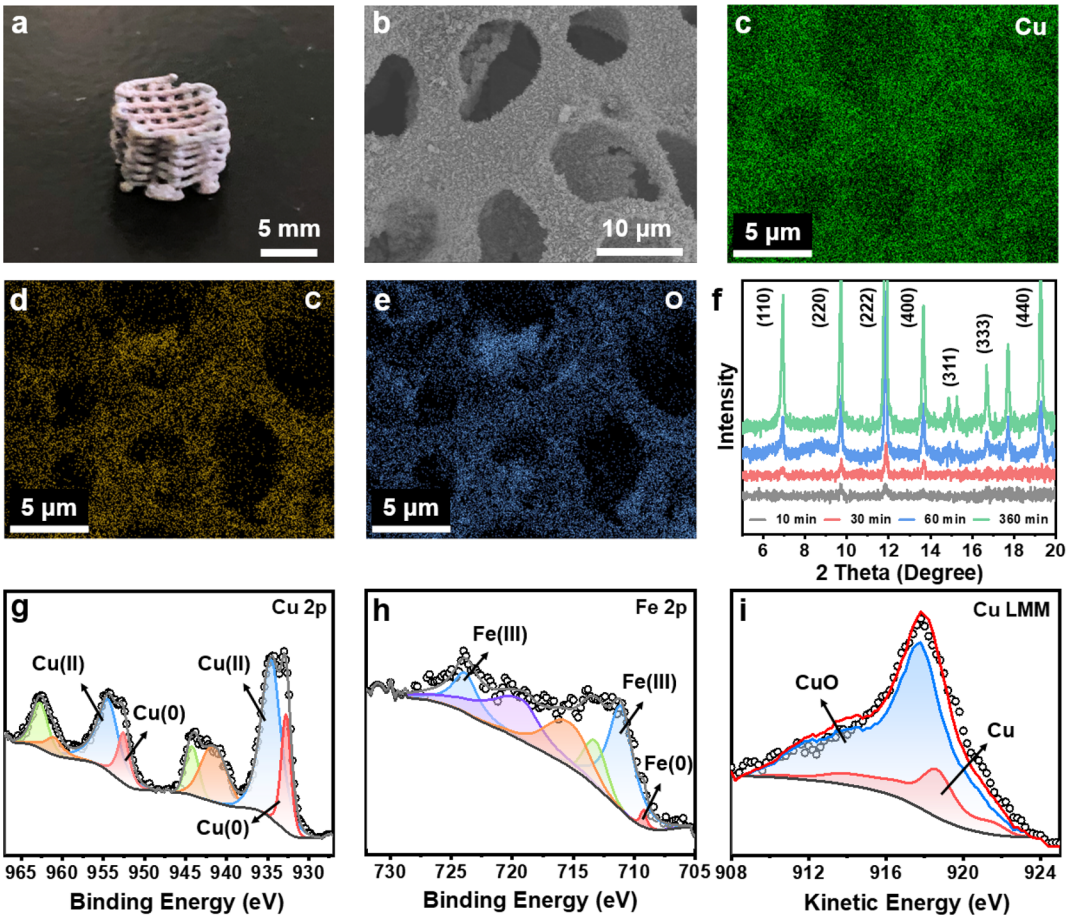

Figure 5. Hierarchical porous HKUST-1@3DPCu4Fe6-R catalyst. (a) Optical images. (b) SEM image. (c−e) EDS elemental mapping results for Cu, C, and O, respectively. (f) XRD patterns of HKUST-1@Cu catalyst with different reaction time. (g−i) XPS fine spectrum of Cu 2p, Fe 2p, and Cu LMM.

https://doi.org/10.1021/cbe.4c00001
Chem Bio Eng. 2024, 1, 264−273

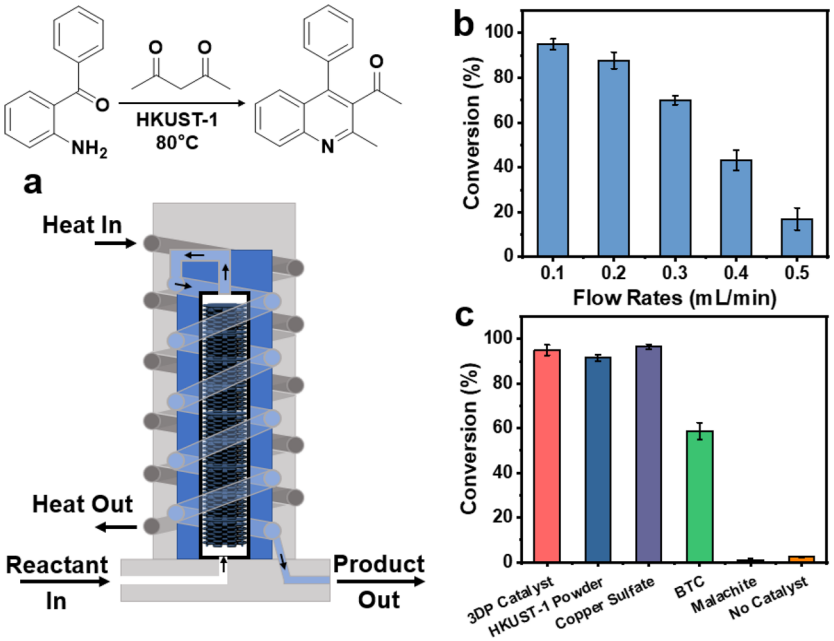

Figure 6. (a) Schematic illustration of the fixed bed microreactor set-up for Friedländer cyclization reaction using HKUST-1@3DPCu4Fe6-R. Reaction conversion with different (b) flow rates and (c) catalysts.

hydrogen donor (i.e., $NaBH_4$). Thus, 3DPCu4Fe6-R catalyst shows greatly enhanced performances in both the apparent rate constant (k_{app}) and TOF.[27]

We further implemented the 3DPCu4Fe6-R catalyst into a columnar flow reactor (Figure 4d inset). The reaction solution flows through the packed catalyst by gravity. We found that when the pristine 4-NP concentration is 0.26 mM, a high apparent kinetic constant (k_{app}) of 86.5×10^{-3} s^{-1} can still be obtained even at a residence time of 2 s (Table S1). Relative to the prior measurements, the TOF and k_{nor} decrease because a 3D-printed structural catalyst is used, which brings almost 10 times the catalyst dosage than the batch reactor. However, the alternative transverse grids of 3DPCu4Fe6-R catalyst also introduce a tortuous path that promotes the mixing of the reactant and product while accelerating the mass transfer between the products on the reactive sites and the reactants in the bulk phase. In addition, 3DPCu4Fe6-R also exhibits consistent performance in the flow reactor for at least five consecutive runs. This mainly stems from the lower metal dissolution characteristics of 3DPCu4Fe6-R. According to the ICP-OES results (Figure S9), in the 4-NP reduction over five cycles, the Cu ion was hardly detected in the reaction liquid. Fe ion was only partially dissolved in the initial two cycles, after which its concentration remained relatively stable. This partial dissolution of Fe may originate from the Fe(III)/Cu and Fe(II)/Cu during reaction. Compared with recent reports on metallic catalysts for 4-NP reduction (Figure 4e), 3DPCu4Fe6-R possesses both significantly wider adaptability of substrate concentration and better catalytic efficiency.

3D-Printed Self-Supported HKUST-1@Cu Catalyst for Fixed Bed Flow Microreactor. Inspired by the unique bimetallic catalytic mechanism of Cu−Fe, we further functionalized 3DPCu4Fe6-R with metal−organic frameworks (MOFs) to explore its functionality. Traditionally, directly growing MOFs on bare metal surfaces requires oxidants (such as sodium persulfate[28]) or precursors (such as nanowires[29]) to create metal ions so that they can be further coordinated with the ligands. This process also requires high temperature or aqueous environments.[30] In this work, surprisingly, we found that MOF crystals can be directly grown on the metal surface (Cu−Fe alloy) in the presence of only the ligand and solvent. Moreover, the ligand solution can be reused for additional rounds of modification.

To modify the MOFs, we put 3DPCu4Fe6-R directly into the 1,3,5-benzenetricarboxylic acid (BTC) ethanol solution (10 mg/mL) and heated it at 80 °C for 30 min. A bluish-gray sample was obtained, indicating that HKUST-1 crystals were successfully modified on the surface (Figure 5a). Further observation under SEM reveals that HKUST-1 crystals are evenly distributed with nanometer size (0.3−1 μm) (Figure 5b). EDS analysis confirms that Cu, C, and O elements on its surface mostly originated from HKUST-1 and the Cu substrate (Figure 5c−e). X-ray photoelectron spectroscopy (XPS) results (Figure 5g−i) show that Cu was in the valence state of +2 and 0, corresponding to the Cu atom in HKUST-1 and 3DPCu4Fe6-R. We also detected that the surface contains very small amounts of Fe, which are in the valence state of +3 and 0, suggesting that Fe in 3DPCu4Fe6-R may also participate in the coordination.

Furthermore, we investigated the effect of the reaction time on the growth of HKUST-1 crystals. As shown in Figure S10, we found that tiny crystal particles (50−100 nm) begin to appear on the 3DPCu4Fe6-R surface after the reaction goes on for 5 min. With the increase of reaction time, the crystal size increases gradually. After 30 min, the crystal size reaches around 0.5−1 μm. The corresponding XRD results confirm that these tiny crystals are HKUST-1 that mainly grow along the two crystal planes (110) and (111), which is consistent with the rod-shaped morphology under SEM (Figure 5f). To elucidate the coordination mechanism between BTC and the 3DPCu4Fe6-R surface, we propose a three-step reaction mechanism (Figure S11): at high temperature, BTC will react with Fe(0) to produce Fe(III) due to its acidity; meanwhile, Fe(III) will react with nearby Cu(0) to form

https://doi.org/10.1021/cbe.4c00001
Chem Bio Eng. 2024, 1, 264−273

Cu(II) and Fe(II); then Cu(II) will coordinate with BTC to form HKUST-1, and Fe(II) will regenerate Fe(III) in the presence of high temperature and oxygen. In the whole process, Fe acts as a catalyst, facilitating the etching of Cu, and eventually HKUST-1 can be directly grown on Cu surfaces.

To further verify our hypothesis, we quantitatively tracked the concentration of Fe and Cu ions in the reaction solution by ICP-OES. As shown in Figure S12 the concentration of Fe ion in the solution increased 10-fold within 300 s, while the concentration of Cu ion remained basically unchanged. As a control (without BTC in the solution), no signal of Fe or Cu ion is detected in the solution after 300 s. According to the above-mentioned theory, due to the continuous etching of Fe by BTC, the concentration of Fe in the final solution will gradually increase. On the other hand, Cu ions will be continuously generated and consumed, which eventually reaches a balance; thus the concentration of Cu ions in the solution will remain steady. Furthermore, it is reported that BTC can also coordinate with Fe(III) to form Fe-BTC;[31] however, in the presence of Cu(II), most BTC will coordinate with Cu preferentially, leaving a small amount of Fe-BTC residuals on the surface, which explains the Fe(III) signals detected by XPS (Figure 5h). 3DPCu4Fe6-R can be regarded as a "self-catalyzed" system during modification. Therefore, if we replenish BTC after each modification cycle, the reaction solution will be reused to modify HKUST-1 (Figure S13).

HKUST-1 has micropores of around 0.9 nm, which shows great catalytic efficiency in Lewis acid-catalyzed reactions.[32] Based on the hierarchical porous 3DPCu4Fe6-R framework, it can be inferred that HKUST-1@3DPCu4Fe6-R should also have an excellent ability to promote mixing as liquids flow through the pores, thereby improving the overall reaction rate and conversion. To prove this, we tested the catalytic performance of HKUST-1@3DPCu4Fe6-R in the Friedländer cyclization reaction. A printed columnar catalyst (Figure 5a) with a diameter of 7 mm perfectly fits the fixed-bed microreactor. 2-Aminobenzophenone (ABP) and acetylacetone (Acac) are chosen to be the model substrates (Figure 6a). The temperature of the whole reactor is controlled (85 °C) in real time. The reaction solution is pumped into the reactor through the micro-mixer module. The final product is collected after the reaction liquid passed through the reactor. The reaction conversion is calculated according to the ^{1}H-NMR spectrum (Figure S14). As shown in Figure 6b, when the flow rate is 0.1 mL/min, we obtained a high conversion of up to 95%. The conversion drops to 17% at a flow rate of 0.5 mL/min because, with the increase in flow rate, the residence time of reaction liquid in the catalyst bed decreases correspondingly; thus, the conversion will gradually decrease. Another reason for the conversion drop may come from the metal dissolution in HKUST-1@3DPCu4Fe6-R, which primarily originates from the metal centers within the MOF structure (Figure S15).

The HKUST-1@3DPCu4Fe6-R shows similar catalytic activity compared to HKUST-1 powder and anhydrous copper sulfate of the same weight (Figure 6c). However, given that the modification is restrained on the pore surfaces, the amount of active Cu ion in HKUST-1@3DPCu4Fe6-R is far lower than HKUST-1 powders or anhydrous copper sulfate, which proves its high catalytic efficiency per active center. The pore structure in HKUST-1@3DPCu4Fe6-R spans 4 orders of magnitude, which increases back-mixing, thus enabling the reactants and products to exchange rapidly between the active center and bulk phase. At the same time, HKUST-1 nanocrystals on the pore surface provide more active sites for the reaction, greatly increasing the catalytic efficiency.

CONCLUSION

In this work, we reported a Cu/Fe composite ink that can be 3D-printed to produce a hierarchical porous metallic structure with pore sizes spanning over 4 orders of magnitude. Such metallic parts are derived by a simple 4-step fabrication strategy: printing, annealing, dealloying, and reannealing. The annealing process makes the pore surface covered with a layer of Cu−Fe alloy, which endows it with great catalytic ability and versatile functionality. Moreover, the hierarchical porous structure promotes mass transfer between reactants and active sites and enhances mixing, thereby greatly improving the catalytic efficiency in fixed-bed reactors. As a demonstration, we first printed out the 3DPCu4Fe6-R catalyst for a gravitational fixed-bed flow reactor and used it to catalyze 4-NP reduction. The 3DPCu4Fe6-R shows an extraordinary catalytic efficiency with an excellent reaction rate constant (k_{app} = 86.5 × 10^{-3} s^{-1}), a high TOF (4.284 h^{-1}), and a wide adaptability of the substrate (up to 1.26 mM). Based on the Cu−Fe alloy feature on the pore surface, we accomplished the direct growth of HKUST-1 onto the 3DPCu4Fe6-R using a mild temperature (80 °C) without the need of an oxidant. The as-prepared HKUST-1@3DPCu4Fe6-R catalyst is then proven to be a highly efficient catalyst for fixed-bed microreactors in catalyzing the Friedländer cyclization. Conversion is over 95% with a retention time of only 20 min. The use of bimetallic particles as printing inks shows great potential in the preparation of hierarchical porous metallic materials. Meanwhile, the use of bimetallic alloys in catalysis to realize surface modifications also provides valuable insights into the functionalization of 3D-printed metallic materials.

EXPERIMENTAL SECTION

Copper/Iron (Cu/Fe) Ink Preparation. Cu powder (99.9% 5000 mesh, Aladdin, Shanghai, China), Fe powder (99.5% 325 mesh, Aladdin, Shanghai, China), and methylcellulose (1500 mPa s, Aladdin, Shanghai, China) were mixed based on molar ratio. Afterward, a certain amount of water was added, and the whole mixture was mechanically stirred until homogenized. Typical formulations are listed in Table S1. Then the Cu/Fe ink was centrifuged (2000 rpm, 30 s) to remove air bubbles and stored in a 4 °C fridge before use.

3D Printing. The Cu/Fe ink was loaded into a 50 mL dispense syringe barrel at 40 kPa attached to an auger pump dispenser. Certain 3D structures were printed by a commercial three-axis system (ZCC2000, ZCC Co., Xiamen, China) through a 300 μm nozzle on a glass slide. The print speed and layer height were optimized as 5 mm/s and 200 mm, respectively. After printing, the sample was thoroughly dried in an oven at 50 °C overnight.

Post-treatments. The printed samples were thermally annealed at 1100 °C (heating rate: 10 °C/min) for 6 h in an argon atmosphere (30 sccm) to form a partially alloyed structure in a tube furnace. After annealing, samples were washed with ethanol and bath sonicated (40 W) to remove impurities. Then the samples were rinsed with deionized water and immersed in 3 M HCl overnight for 24 h for the dealloying process. Afterwards, the samples were washed with deionized water thoroughly and vacuum-dried (0.1 bar, 50 °C). A reannealing process was applied by reheating the samples in a tube furnace at 850 °C (heating rate: 10 °C/min) under an argon atmosphere (30 sccm). The samples after each post-treatment step were denoted according to Cu/Fe molar ratio and followed by suffixes A (annealed), D (dealloyed), and R (reannealed), respectively (e.g.,

https://doi.org/10.1021/cbe.4c00001
Chem Bio Eng. 2024, 1, 264−273

Cu4Fe6-R). As long as it is specifically mentioned, samples without suffixes are considered those after the reannealing procedure.

HKUST-1@3DPCu4Fe6-R Preparation. 3DPCu4Fe6-R was added into 10 mg/mL 1,3,5-benzenetricarboxylic acid (BTC) ethanol solution in a sealed reaction tube. The whole reactionware was heated to 80 °C for different periods of time to ascertain the growth mechanism. After the reaction, the samples were rinsed with ethanol to remove excess ligands and dried in an oven (50 °C).

4-Nitrophenol (4-NP) Reduction. For 4-NP reduction, 3DPCu4Fe6-R was put into a homemade tubular flow reactor (i.d. 10 mm). The 4-NP (99.9%, Aladdin, Shanghai, China) and $NaBH_4$ (99.9%, Aladdin, Shanghai, China) stock solutions were mixed and then immediately poured into a tubular reactor to initiate the reaction. The product was gathered in a glass vial and tested by a UV−vis spectrometer without any further treatment. The reaction kinetics are calculated based on the absorbance at 400 nm according to the literature.[33]

Friedländer Cyclization. For Friedländer condensation of 2-aminobenzophenone (2-ABP, 98%, Aladdin, Shanghai, China) and acetylacetone (Acac, 99%, Aladdin, Shanghai, China), a solvent-free route was applied according to the literature.[34] HKUST-1@3DPCu4Fe6-R catalyst was put into the modular microreaction system (F200, Ehrfeld Mikrotchnik GmbH, Germany) after thermal activation at 110 °C. Then the mixture of 2-ABP and Acac with a molar ratio of 1 to 5 was pumped into the reaction system (85 °C) to initiate the reaction. After the reaction, the product solution was treated with ethanol, and then the solvent was removed under vacuum. The solid was dissolved in dichloromethane, filtered to further remove impurities, and then dried under vacuum. The catalytic activity was analyzed by ^{1}H-NMR spectra (400 MHz, ECX-400, JEOL, Japan) of the products in deuterated chloroform ($CDCl_3$). The peaks for calculating the conversion were from signals at around 7.2 and around 8.1 ppm.

Characterization. The morphology of the printed catalyst was observed by scanning electron microscopy (SEM, S8100, Hitachi, Japan). Porosity and specific area were measured by mercury intrusion porosimetry (MIP, AutoPore Iv-9510, Micromeritics, USA). X-ray diffraction (D8-focus, Bruker, German) was used to determine the crystalline composition of the printed catalyst. X-ray photoelectron spectroscopy (XPS, PHI1600 ESCA, PerkinElmer, USA) was used to analyze the element valence change during the growth of HKUST-1. The rheology of the Cu/Fe inks was measured using a rotary rheometer (DHR-2, TA Instruments, USA) in oscillation mode (strain, 1%; frequency, 10 Hz).

■ ASSOCIATED CONTENT

Supporting Information

The Supporting Information is available free of charge at https://pubs.acs.org/doi/10.1021/cbe.4c00001.

Ink formulation, SEM images, linear shrinkage ratio, compressive stress curve, phase diagram, calculation results, porosity of samples, UV−vis absorption curve, comparison of catalytic performance, ICP-OES results, illustrations of a possible mechanism for the direct growth of HKUST-1 on porous Cu structure, ^{1}H-NMR spectra (PDF)

■ AUTHOR INFORMATION

Corresponding Authors

Ruizhe Xing − *School of Chemistry and Chemical Engineering, Northwestern Polytechnical University, Xi'an 710072, P. R. China; Department of Chemical and Biomolecular Engineering, North Carolina State University, Raleigh, North Carolina 27695, United States; School of Chemical Engineering and Technology, Tianjin University, Tianjin 300072, P. R. China*; Email: rzxing@nwpu.edu.cn

Renliang Huang − *School of Marine Science and Technology, Tianjin University, Tianjin 300072, P. R. China*; orcid.org/0000-0003-0797-3473; Email: tjuhrl@tju.edu.cn

Michael D. Dickey − *Department of Chemical and Biomolecular Engineering, North Carolina State University, Raleigh, North Carolina 27695, United States*; orcid.org/0000-0003-1251-1871; Email: mddickey@ncsu.edu

Authors

Rongxin Su − *School of Marine Science and Technology, Tianjin University, Tianjin 300072, P. R. China*; orcid.org/0000-0001-9778-9113

Jie Kong − *School of Chemistry and Chemical Engineering, Northwestern Polytechnical University, Xi'an 710072, P. R. China*; orcid.org/0000-0002-9405-3204

Wei Qi − *School of Chemical Engineering and Technology, Tianjin University, Tianjin 300072, P. R. China*; orcid.org/0000-0002-7378-1392

Complete contact information is available at: https://pubs.acs.org/10.1021/cbe.4c00001

Author Contributions

The manuscript was written through contributions of all authors. All authors have given approval to the final version of the manuscript.

Notes

The authors declare no competing financial interest.

■ ACKNOWLEDGMENTS

The authors acknowledge the support from the Hai'an & Taiyuan University of Technology Advanced Manufacturing and Intelligent Equipment Industry Institute (2023HA-TYUTKFYF027) and the National Natural Science Foundation of China (52203101).

■ REFERENCES

(1) Tappan, B. C.; Steiner, S. A., III; Luther, E. P. Nanoporous metal foams. *Angew. Chem. Int. Ed* **2010**, *49* (27), 4544−4565.

(2) Snyder, J.; Fujita, T.; Chen, M. W.; Erlebacher, J. Oxygen reduction in nanoporous metal-ionic liquid composite electrocatalysts. *Nat. Mater.* **2010**, *9* (11), 904−907.

(3) Zhu, C.; Qi, Z.; Beck, V. A.; Luneau, M.; Lattimer, J.; Chen, W.; Worsley, M. A.; Ye, J.; Duoss, E. B.; Spadaccini, C. M. Toward digitally controlled catalyst architectures: Hierarchical nanoporous gold via 3D printing. *Sci. Adv.* **2018**, *4* (8), No. eaas9459.

(4) Nguyen, N. T.; Ozkan, S.; Tomanec, O.; Zhou, X.; Zboril, R.; Schmuki, P. Nanoporous AuPt and AuPtAg alloy co-catalysts formed by dewetting−dealloying on an ordered TiO2 nanotube surface lead to significantly enhanced photocatalytic H2 generation. *J. Mater. Chem. A* **2018**, *6* (28), 13599−13606.

(5) Du, R.; Jin, X.; Hübner, R.; Fan, X.; Hu, Y.; Eychmüller, A. Engineering Self-Supported Noble Metal Foams Toward Electrocatalysis and Beyond. *Adv. Energy Mater.* **2020**, *10* (11), 1901945.

(6) Huang, X.; Chang, S.; Lee, W. S. V.; Ding, J.; Xue, J. M. Three-dimensional printed cellular stainless steel as a high-activity catalytic electrode for oxygen evolution. *J. Mater. Chem. A* **2017**, *5* (34), 18176−18182.

(7) Pang, F.; Wang, Z.; Zhang, K.; He, J.; Zhang, W.; Guo, C.; Ding, Y. Bimodal nanoporous Pd3Cu1 alloy with restrained hydrogen evolution for stable and high yield electrochemical nitrogen reduction. *Nano Energy* **2019**, *58*, 834−841.

(8) Trogadas, P.; Nigra, M. M.; Coppens, M.-O. Nature-inspired optimization of hierarchical porous media for catalytic and separation processes. *New J. Chem.* **2016**, *40* (5), 4016−4026.

(9) Qi, Z.; Weissmüller, J. r. Hierarchical nested-network nanostructure by dealloying. *ACS Nano* **2013**, *7* (7), 5948−5954. Qi, Z.; Vainio, U.; Kornowski, A.; Ritter, M.; Weller, H.; Jin, H.; Weissmüller, J. Porous gold with a nested-network architecture and ultrafine structure. *Adv. Funct. Mater.* **2015**, *25* (17), 2530−2536.
(10) Lee, M. N.; Santiago-Cordoba, M. A.; Hamilton, C. E.; Subbaiyan, N. K.; Duque, J. G.; Obrey, K. A. Developing Monolithic Nanoporous Gold with Hierarchical Bicontinuity Using Colloidal Bijels. *J. Phys. Chem. Lett.* **2014**, *5* (5), 809−812.
(11) Kitson, P. J.; Glatzel, S.; Chen, W.; Lin, C.-G.; Song, Y.-F.; Cronin, L. 3D printing of versatile reactionware for chemical synthesis. *Nat. Protoc* **2016**, *11* (5), 920−936.
(12) Symes, M. D.; Kitson, P. J.; Yan, J.; Richmond, C. J.; Cooper, G. J.; Bowman, R. W.; Vilbrandt, T.; Cronin, L. Integrated 3D-printed reactionware for chemical synthesis and analysis. *Nat. Chem.* **2012**, *4* (5), 349−354.
(13) Azuaje, J.; Tubío, C. R.; Escalante, L.; Gómez, M.; Guitián, F.; Coelho, A.; Caamaño, O.; Gil, A.; Sotelo, E. An efficient and recyclable 3D printed α-Al2O3 catalyst for the multicomponent assembly of bioactive heterocycles. *Appl. Catal. A - Gen* **2017**, *530*, 203−210.
(14) Wehinger, G. D.; Heitmann, H.; Kraume, M. An artificial structure modeler for 3D CFD simulations of catalytic foams. *Chem. Eng. J.* **2016**, *284*, 543−556.
(15) Stuecker, J. N.; Miller, J. E.; Ferrizz, R. E.; Mudd, J. E.; Cesarano, J. Advanced support structures for enhanced catalytic activity. *Ind. Eng. Chem. Res.* **2004**, *43* (1), 51−55.
(16) Yang, C.; Zhang, C.; Xing, W.; Liu, L. 3D printing of Zr-based bulk metallic glasses with complex geometries and enhanced catalytic properties. *Intermetallics* **2018**, *94*, 22−28.
(17) Zhang, Y.; Sun, X.; Nomura, N.; Fujita, T. Hierarchical Nanoporous Copper Architectures via 3D Printing Technique for Highly Efficient Catalysts. *Small* **2019**, *15* (22), No. e1805432.
(18) Losey, M. W.; Jackman, R. J.; Firebaugh, S. L.; Schmidt, M. A.; Jensen, K. F. Design and fabrication of microfluidic devices for multiphase mixing and reaction. *J. Microelectromech. Syst* **2002**, *11* (6), 709−717.
(19) Xing, R.; Yang, J.; Zhang, D.; Gong, W.; Neumann, T.V.; Wang, M.; Huang, R.; Kong, J.; Qi, W.; Dickey, M.D. Metallic gels for conductive 3D and 4D printing. *Matter* **2023**, *6* (7), 2248−2262.
(20) Salje, G.; Feller-Kniepmeier, M. The diffusion and solubility of iron in copper. *J. Appl. Phys.* **1978**, *49* (1), 229−232.
(21) Anand, M. S.; Agarwala, R. P. Diffusion of Copper in Iron. *J. Appl. Phys.* **1966**, *37* (11), 4248−4251.
(22) Kuper, A.; Letaw, H.; Slifkin, L.; Sonder, E.; Tomizuka, C. T. Self-Diffusion in Copper. *Phys. Rev.* **1954**, *96* (5), 1224−1225.
(23) Turchanin, M.A.; Agraval, P. G. Cohesive Energy, Properties, and Formation Energy Of Transition Metal Alloys. *Powder Metall. Met. Ceram* **2008**, *47*, 26−39.
(24) Zhang, K.; Liu, Y.; Deng, J.; Xie, S.; Lin, H.; Zhao, X.; Yang, J.; Han, Z.; Dai, H. Fe2O3/3DOM BiVO4: High-performance photocatalysts for the visible light-driven degradation of 4-nitrophenol. *Appl. Catal. B - Environ* **2017**, *202*, 569−579.
(25) Tranchant, M.; Serrà, A.; Gunderson, C.; Bertero, E.; García-Amorós, J.; Gómez, E.; Michler, J.; Philippe, L. Efficient and green electrochemical synthesis of 4-aminophenol using porous Au micropillars. *Appl. Catal. A - Gen* **2020**, *602*, No. 117698.
(26) Xu, Z.; He, X.; Liang, M.; Sun, L.; Li, D.; Xie, K.; Liao, L. Catalytic reduction of 4-nitrophenol over graphene supported Cu@Ni bimetallic nanowires. *Mater. Chem. Phys.* **2019**, *227*, 64−71.
(27) Park, J.; Saratale, G. D.; Cho, S.-K.; Bae, S. Synergistic effect of Cu loading on Fe sites of fly ash for enhanced catalytic reduction of nitrophenol. *Sci. Total. Environ* **2020**, *705*, No. 134544.
(28) Ji, H.; Hwang, S.; Kim, K.; Kim, C.; Jeong, N. C. Direct in situ conversion of metals into metal−organic frameworks: a strategy for the rapid growth of MOF films on metal substrates. *ACS Appl. Mater. Interfaces* **2016**, *8* (47), 32414−32420.
(29) Liu, T.; Li, P.; Yao, N.; Kong, T.; Cheng, G.; Chen, S.; Luo, W. Self-sacrificial template-directed vapor-phase growth of MOF assemblies and surface vulcanization for efficient water splitting. *Adv. Mater.* **2019**, *31* (21), No. 1806672.
(30) Zheng, Y.; Qiao, S.-Z. Direct growth of well-aligned MOF arrays onto various substrates. *Chem.* **2017**, *2* (6), 751−752.
(31) Wezendonk, T. A.; Santos, V. P.; Nasalevich, M. A.; Warringa, Q. S.; Dugulan, A. I.; Chojecki, A.; Koeken, A. C.; Ruitenbeek, M.; Meima, G.; Islam, H.-U. Elucidating the nature of Fe species during pyrolysis of the Fe-BTC MOF into highly active and stable Fischer−Tropsch catalysts. *ACS Catal.* **2016**, *6* (5), 3236−3247.
(32) Chui, S. S.-Y.; Lo, S. M.-F.; Charmant, J. P.; Orpen, A. G.; Williams, I. D. A chemically functionalizable nanoporous material [Cu3 (TMA) 2 (H2O) 3] n. *Science* **1999**, *283* (5405), 1148−1150.
(33) Huang, R.; Zhu, H.; Su, R.; Qi, W.; He, Z. Catalytic Membrane Reactor Immobilized with Alloy Nanoparticle-Loaded Protein Fibrils for Continuous Reduction of 4-Nitrophenol. *Environ. Sci. Technol.* **2016**, *50* (20), 11263−11273.
(34) Perez-Mayoral, E.; Musilova, Z.; Gil, B.; Marszalek, B.; Polozij, M.; Nachtigall, P.; Cejka, J. Synthesis of quinolines via Friedlander reaction catalyzed by CuBTC metal-organic-framework. *Dalton Trans* **2012**, *41* (14), 4036−4044.

https://doi.org/10.1021/cbe.4c00001
Chem Bio Eng. 2024, 1, 264−273